shared robot-human route after taking over an autonomous ground vehicle

Padmalochan Nayak [1], Lingaraj Nath [2], Jagdish Prasad Pradhan [3], Bibhudatta Panigrahi [4], Rajiba Nayak [5]
E SUJITH PRASAD[6]
[1, 2, 3, 4, 5] Gandhi Institute for Education & Technology, Baniatangi, Khordha, Odisha
[6]NM Institute of Engineering & Technology,Bhubaneswar,Odisha

padmalochannayak@giet.edu.in, lingarajnath@giet.edu.in, jagdishppradhan@giet.edu.in, bdpanigrahi@giet.edu.in, rajibanayak@giet.edu.in

A R T I C L E I N F O

Keywords:
Shared human–robot control
Human robot interaction
Path following
Unmanned vehicles
Super-twisting sliding mode control

A B S T R A C T

This study examines the shared route that results from a single person operating an autonomous ground vehicle. In a mixed initiative method, the human and machine inputs are combined using a passive assessment of human purpose. To prevent external disturbances through comparable control, the blending law is paired with saturated super-twisting sliding mode speed and heading controllers. It has been demonstrated that when the suggested blending law is employed, the combined control signals from the automated controller and the human controller follow the mechanical actuator magnitude limits. In order to illustrate the methodology, shared control experiments are carried out with an autonomous ground vehicle that travels along a route resembling a lawnmower.

1. Introduction

Unmanned vehicles are often deployed in complex, dynamic and highly unstructured environments. Automatic control may be required to achieve consistent behaviors and reliably reject disturbances, but humans are inherently better at responding to novel situations requiring higher-level reasoning. In shared human–robot control, the robot operates semi-autonomously, and the responsibility for task execution is shared. The challenge is to appropriately combine the inputs from both a human and an automatic control system in order to take advantage of their complementary strengths.

Shared control [1,2], can sometimes be the only viable solution to deal with the complexity and unpredictability of real-world scenarios [3]. Examples of applications where shared control can be beneficial include: infrastructure survey and mapping [4,5]; environmental monitoring and survey [6–8]; agriculture [9,10]; and healthcare [11, 12].

In this paper, the focus is on the implementation of shared control involving a single machine and one person, jointly performing a common task. The type of shared control in which a human can interfere with the autonomous control of a system is known as a mixed-initiative interaction. A common example of this type of shared control is an automobile driver assist system [13–16]. Ideally, according to the H-metaphor, the interaction between a human and machine would have characteristics similar to the interaction between a well-trained horse and an experienced rider [17–19], which is paraphrased here as follows: The horse has much stronger and faster abilities in movement, but the human usually has a higher control authority except in emergency situations, where the horse already reacts before the human might even be aware of a danger. The human can control the horse quite directly with a tight rein, or more indirectly with a loose rein. Even with a loose rein, the human will keep a majority of the responsibility.

Even a seemingly simple scenario of a single human interacting with a single machine can be difficult to analyze from a control theoretic standpoint. An important question is how to best blend the control inputs from the human with those from the machine. Denote the human control input as $u_h(t)$ and the input from an automatic controller as $u_a(t)$. A linear blending law is often used, such as

$$u(t) = A_h u_h(t) + A_a u_a(t), \quad A_h + A_a = I, \tag{1}$$

where $u(t)$ is the total control input, A_h and A_a are arbitration matrices, and I is the identity matrix [1]. The basic idea is that two control inputs with complementary capabilities (human and robot) are adaptively combined by means of the arbitration matrices, to obtain an overall controller of improved performance. If the blending law is appropriately selected, the resulting controller should perform as well as, or better, than the best individual component. By using a blending law based on a convex function pair, the case that the two controllers operate independently of each other and according to their own rules is included, while still permitting the controllers to work in combination, when more effective. There are many ways in which the arbitration matrices can be selected. For example, [20,21] shift the control of a shared system from human to machine by taking $□_h = □$ and $□_□ = 1 - □_h$ and using hysteresis-based switching to set the value of □ to either 0 or 1, depending upon whether a set of safety metrics lies within a safe set, a hysteresis set, or an unsafe set, as well as the direction in which the safety metrics transition between sets (e.g. from safe to hysteresis or vice versa). Other approaches to blending the human and machine inputs include the use of probabilistic models of efficiency, mission risk or human safety [22], or drift–diffusion decision-making models [11,23]. Lastly, in [14,15], a blending methodology is based on the cooperative relationship between the human operator and automated system in a car Lane-Keeping Assist System (LKAS). A metric of the cooperative status between the driver and the automated steering system is constructed using a pseudo-power pair of the torque from each agent and the vehicle's lateral velocity. A control method that enables drivers to change lanes smoothly is proposed based on the estimated cooperative status.

Here, we propose a shared control approach for path following or trajectory tracking that utilizes the following main features:

1. The use of a storage function $□_h$ (to be defined below) to determine human intent. The passivity of a teleoperated system contains a component arising from the power input by a human actuating some sort of interface, such as a joystick, and a second component associated with the power expended by the robot in moving against externally applied forces [24]. We assume the human input required to counteract external forces acting on the system is negligible. This permits the passive measure of human intent to be based solely on the human component.
2. A linear blending law (1), which incorporates an exponential function that takes the measure of human intent $□_h$ as its argument, i.e. $□_h \propto (1 - e^{-□_h})$ and $□_□ \propto e^{-□_h}$, so that the system quickly and smoothly transitions between automatic control and human control.
3. The inclusion of actuator magnitude limits in the design of the machine (automatic) controller.

The proposed approach is experimentally implemented for the human–machine shared control of a path-following unmanned ground vehicle (UGV). The machine control uses super-twisting second order sliding mode controllers for the speed and heading control of the UGV. The human input is obtained using a force-reflexive joystick. The shared control system is tested on a lawn mower pattern shaped search path for three scenarios related to the H-Metaphor described above.

1.1. Contributions

The first main contribution of this paper is the formulation of a novel storage function and its use as a measure of human intent. The storage function was selected because of its relation to the definition of passivity in human–machine systems, especially for systems involving teleoperation, see for example [24,25]. It is also similar to the concept of the pseudo work used in lane keeping assist systems [14]. However, the storage function proposed here is quite different, as it is only dependent on the human side of the interconnected human–machine system.

The second main contribution of this work is the proposed exponential function based blending law, which is also novel. The proposed blending law is easy to implement, as it simply takes the storage function as its argument, and permits the human–machine system to rapidly and smoothly switch between human and machine control.

The third main contribution of the work is that it is explicitly proven that, if the design of the machine controller respects the magnitude limits of the systems actuators, the shared control signal from both the human and machine also respects the actuator magnitude limits when the proposed blending rule is used. Thus, the stability of the shared control is explicitly addressed by quantifying the acceptable actuator magnitude constraints relative to the magnitude of anticipated disturbances, taking the constraints into account during control design and demonstrating that the shared signal also respects these constraints. We note that guaranteeing the stability of share human–robot control is, in general, a largely open research question [1], which is not always explicitly addressed by papers on shared control in the literature.

Lastly, the approach is illustrated via the experimental implementation of a shared path following control system on a UGV performing a search across a large test area. It should be noted that most recent work involving shared control, such as lane keeping assist systems, or medical assistive systems, focus on systems in which the human and machine are either in direct physical contact, or located very near to one another.

The work presented here extends the concepts introduced by the authors in the conference publication [26]. The present paper adds to that paper in the following important ways: the proposed shared control approach is extended from a single input, single output system to a multiple input, multiple output system; the shared control approach is experimentally implemented on a physical platform; and, while the original approach proposed in [26] makes use of a nonlinear disturbance observer (NDO) and geometric rescaling of the machine control input to ensure that actuator magnitude constraints are respected, it is shown in the present paper that the same control objectives can be satisfied using saturated super twisting sliding mode control, in which the equivalent control signal from the higher order sliding mode term acts similarly to the feedforward, disturbance canceling, control input from an NDO and the saturation of the control inputs performs the same role as geometric rescaling; lastly, here it is proven that when the proposed blending law is used, the shared control signal from both human and machine respects actuator magnitude constraints.

1.2. Organization

The organization of the remainder of the paper is as follows. A dynamical model of the UGV and main assumptions are presented in Section 2, details of the shared controller design are shown in Section 3, the experimental methods and instrumentation are described in Section 4, the main experimental results are discussed in 5 and, lastly, the main conclusions are provided in Section 6.

2. Problem formulation

The motion of the robot is assumed to be constrained to the horizontal plane with only three degrees of freedom (DOF): longitudinal (surge), lateral (sway) and yaw. The three DOF kinematic equations reduce to

$$\dot{□} = (), \tag{2}$$

where □ is the heading angle of the vehicle, □(□) is the transformation matrix from the body-fixed system to a North-East-Down (NED) inertial coordinate system, which is given by

$$□(□) := \begin{bmatrix} \cos □ & -\sin □ & 0 \\ \sin □ & \cos □ & 0 \\ 0 & 0 & 1 \end{bmatrix} \in (3), \tag{3}$$

and

$$□ := \begin{pmatrix} □_□ \\ □_□ \\ □ \end{pmatrix} \in \mathbb{R}^{2} \times, \quad \text{and} \quad □ := \begin{pmatrix} □ \\ □ \\ □ \end{pmatrix} \in \mathbb{R}^3 \tag{4}$$

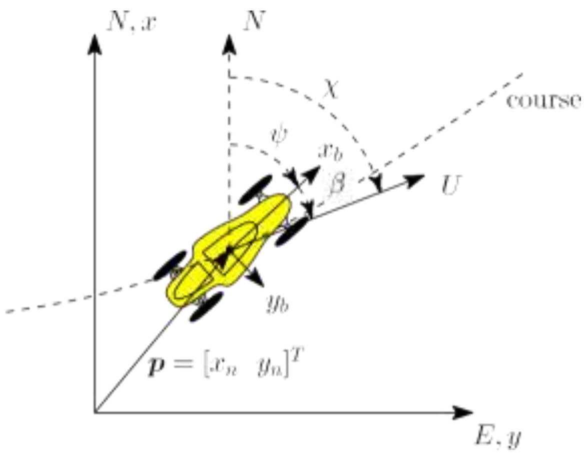

Fig. 1. 3 DOF maneuvering coordinate system definitions.

Table 1
Variables used in (5)–(8).

Term	Dimension	Description
M	$\mathbb{R}^3 \times \mathbb{R}^3$	Inertia tensor
C(v)	$\mathbb{R}^3 \times \mathbb{R}^3$	Coriolis and centripetal matrix
D(v)	$\mathbb{R}^3 \times \mathbb{R}^3$	Damping matrix
□	$\mathbb{R}^3$	Actuator forces/moments
d	$\mathbb{R}^3$	Disturbance forces/moments

are the position and orientation (pose) vector and velocity vector (in body-fixed coordinates), respectively (see Fig. 1). Here, the symbol $\mathbb{R}^{□}$ is the Euclidean space of dimension □, ⋅ is an Euler angle defined on the interval [−□, □], and (3) is the Special Orthogonal group of order 3. Thus, □ has three components, which represent two linear displacements and one angular rotation. The variables appearing in (4) include position Northward □, position Eastward □, surge speed □, sway speed □ and yaw rate □.

The dynamic equations of motion are given by

$$□□̇ + □(□)□ + □(□)□ = □ + □. \tag{5}$$

where

$$□ := \begin{bmatrix} □ & 0 & 0 \\ 0 & □ & 0 \\ 0 & 0 & □ \end{bmatrix}, \tag{6}$$

$$□(□) := \begin{bmatrix} 0 & 0 & -□□ \\ 0 & 0 & □□ \\ □□ & -□□ & 0 \end{bmatrix}, \tag{7}$$

$$□(□) := \begin{bmatrix} -□|□| & 0 & 0 \\ 0 & 0 & 0 \\ 0 & 0 & 0 \end{bmatrix}. \tag{8}$$

where □ is the mass of the vehicle, □ is the mass moment of inertia about the □ axis, and □ < 0 is the drag coefficient along the □ axis. The remaining terms appearing in (5)–(8) are defined in Table 1.

Remark 1. In this work, a dynamic model of the UGV is used, rather than a kinematic model. Kinematic vehicle models are most accurate when good ground contact is assured, so that it can be assumed the vehicle's wheels roll without any lateral slippage (i.e., slippage perpendicular to the plane of the disk of each wheel). The maximum lateral force produced by a wheel is given by $□^{max}$ = □□, where □ is the friction coefficient between the tire and the ground, and □ is the normal load on the tire [27].

Consider the operation of a UGV at a forward speed of $□_{max}$ = 2 m/s performing a turn with a constant radius of $□_{min}$ = 1.5 m. Take = the wheels on the inside of the turn and slightly higher on the wheels on the outside of the turn). Let the coefficient of friction be □ = 0.5, which is often used to model a surface with loose gravel [27]. Assuming the UGV is operating on level ground, the approximate ratio of the centrifugal force of the UGV acting on each wheel to the maximum lateral friction force on each wheel $□^{max}$ is

$$\frac{□□^2_{max}/(4□_{min})}{□□□/4} = 0.54.$$

Thus, when a UGV is operated under these conditions in a sharp turn on level ground, the centrifugal force of the UGV acting on each tire can be a large fraction of the maximum lateral force that can be generated by each tire. Further, if performing such a turn on terrain with a slope of □, the maximum value of the ratio can be approximated as

$$\frac{[□^2_{max}/□_{min} + □\sin(□)]/4}{□□□\cos(□)/4},$$

which gives 1.0 for a slope of 12.5° and 1.5 for a slope of 25°.

It is anticipated that some of the most likely UGV robotics applications to benefit from the use of shared human–robot control will include search & rescue or alpine farming applications, which would sometimes be conducted in rugged, sloped, off-road environments and which could involve the use of small UGVs operating at speeds and turning radii near the ranges of $□_{max}$ and $□_{min}$ given above. Since the magnitude of the expected centrifugal force on each wheel in sharp turns is comparable to that of the maximum lateral friction force on each wheel, it cannot be assured that the UGV's wheels will rotate without lateral slippage. Thus, a dynamic model of the vehicle is used in this work.

Assumption 1. The unknown disturbance vector □ includes exogenous disturbances and unmodeled dynamics. The components of □ and their time derivatives are unknown and time-varying, yet bounded. There exist positive constants □ and □ such that ‖□(□)‖ ≤ □ and ‖□̇(□)‖ ≤ □, where ‖⋅‖ represents the 2-norm of a vector or matrix.

Assumption 2. The actuator forces can be taken as

$$□ = \begin{bmatrix} □ \\ 0 \\ □ \end{bmatrix}, \tag{9}$$

where □ depends on the throttle command only and □ depends on the steering angle only. In reality, the tires generate forces along the □-axis, a moment about the □-axis, and the total tire-generated forces/moments are also coupled through the commanded steering angle and throttle (along all three body-fixed axes). These unmodeled terms are taken to be included in the model uncertainty represented by □ (Assumption 1).

3. Control design

In the next section we construct the automatic controller which steers the vehicle along a time-independent path in the absence of human intervention, as well as provide a description of how the human is included in the control loop. In the sequel, take the components of the disturbance vector to be □ = [□ □] and define the saturation function as

$$\mathrm{sat}_{□_{max}}(□) := \begin{cases} □, & |□| \le □_{max}, \\ □_{max}\,\mathrm{sgn}(□), & |□| > □_{max}, \end{cases}$$

where $□_{max} > 0$ is a constant.

3.1. Machine control

□□/4, where □ is gravitational acceleration (□□ will be slightly lower on

The overall path to be followed consists of a set of □ piecewise linear straightline segments, which are connected by □ + 1 waypoints. When the position of the UGV is within a circle of acceptance of radius R_{k+1} around waypoint p_{k+1} (where $p_k = (x_k, y_k)$), so that

$$(x_n - x_{k+1})^2 + (y_n - y_{k+1})^2 \le R^2_{k+1} \tag{10}$$

a switching mechanism is used to select the next waypoint.

As can be seen from (4) and (9), the UGV is underactuated because its configuration space is three dimensional, i.e., $\dim(\eta) = 3$, but the control inputs τ_x and τ_ψ can only independently generate control efforts in two directions, i.e., a surge force along the x_b axis and a yaw moment about the z_b axis. Since the UGV cannot generate control forces/moments along every degree of freedom in its configuration space, it cannot arbitrarily move from any given initial pose to any given final pose. Instead, the set of intermediate pose configurations that it can pass through when moving from some initial pose to some final pose is limited. Because of this, it is not possible to define a control objective in the full configuration space of the UGV. In robotics, a common strategy for overcoming this problem is to define the control objective in a fully-actuated workspace, i.e., within a set of pose configurations that has the same number of dimensions as the number of independent actuator forces. The Lookahead-Based Steering Method [28–31] is one such strategy. The method assumes that the vehicle is controlled to move at a constant desired forward speed and uses the relative pose (position and heading angle) between the UGV and the nearest path segment being followed to generate a desired heading angle. Thus, the control objective is formulated within a fully-actuated, two dimensional, workspace, i.e., only speed and heading need to be controlled. Since the Lookahead-Based Steering Method only generates the desired speed and heading, rather than the control inputs themselves, it is known as a guidance law. Any suitable control technique (e.g., Proportional Integral Derivative Control, Backstepping Control, Sliding Mode Control) can be applied to make the UGV follow the desired speed and heading.

Here, super-twisting sliding mode controllers are used for both speed- and heading-control. In standard (first order) sliding mode control, a sliding mode variable is constructed using the tracking error of the closed loop system. The control input is typically generated using the sign of the sliding mode variable. As the controller drives the error to zero, the sign of the error (and hence the sliding mode variable) will typically oscillate between positive and negative values, which causes the control input to switch discontinuously at high frequency in a condition known as *chattering*. While first order sliding mode control is generally very robust to disturbances, the high-frequency switching control signal can adversely affect the performance of certain types of actuators. Chattering can be mitigated using various approaches, such as boundary layers [32] or continuous approximations of the sign function [33]. However, in the presence of disturbances such approaches cannot drive the error to zero (causing a loss of robustness/accuracy) and do not converge in finite time. In super-twisting control, a continuous control input is constructed by adding the time integral of a high-frequency switching term to a continuous function, which takes the sliding mode variable as its argument. Effectively, the integral of the high frequency switching term acts to cancel perturbations, while the continuous function drives the sliding mode variable (and hence the closed loop system error) to zero in finite time [33,34].

3.1.1. Surge speed control

Define the surge speed error as

$$\tilde{u} := u - u_d \tag{11}$$

and take the associated sliding surface to be

$$s_u := \dot{\tilde{u}} + \lambda_u |\tilde{u}|^{1/2}\,\mathrm{sgn}(\tilde{u}), \tag{12}$$

where λ_u is a tunable control design parameter. Assume that the sliding surface $s_u = 0$ is reached at time t_r. Once the sliding surface has been reached, the surge speed error will be driven to zero in finite time. To see this note that when $s_u = 0$

$$\dot{\tilde{u}} = -\lambda_u |\tilde{u}|^{1/2}\,\mathrm{sgn}(\tilde{u}). \tag{13}$$

The solution to this differential equation is

$$\tilde{u}(t)^{1/2} - \tilde{u}(0)^{1/2} = -\frac{\lambda_u}{2}t \tag{14}$$

Thus, $\tilde{u}(t) = 0$ in the finite time

$$t_{fs} = \frac{2\sqrt{\tilde{u}(0)}}{\lambda_u}, \tag{15}$$

after the sliding surface has been reached. To accomplish this, take the surge speed controller to be

$$\begin{aligned} \tau_{xs} &= \mathrm{sat}_{\tau_{max}}\left(-k_u|s_u|^{1/2}\,\mathrm{sgn}(s_u) + \tau_{s1}\right), \\ \dot{\tau}_{s1} &= \begin{cases} 0, & |\tau_{xs}| = \tau_{max}, \\ -k_{s1}\,\mathrm{sgn}(s_u), & |\tau_{xs}| < \tau_{max}, \end{cases} \end{aligned} \tag{16}$$

where k_u and k_{s1} are tunable control design parameters, and $\tau_{max} := \max|\tau_x|$ is the maximum surge force that can be produced by the UGV's drive train. Then, using (16) in (5)–(9), the corresponding closed loop error is given by

$$\dot{s}_u = \psi_u + \mathrm{sat}_{\tau_{max}}\left(-k_u|s_u|^{1/2}\,\mathrm{sgn}(s_u) + \tau_{s1}\right), \tag{17}$$

where

$$\psi_u := -\ddot{u}_d + \dots + \lambda_u |\tilde{u}|\,\dots + d_u. \tag{18}$$

According to the concept of *equivalent control* [33,35], τ_{s1} (the integrated value of $\dot{\tau}_{s1}$) becomes equivalent to ψ_u in the finite time t_s driving the closed loop system to the sliding surface and keeping it there. Thus, once on the sliding surface, the closed loop speed error dynamics (17) become the same as the equation for the sliding mode (13) so that the speed error is driven to zero with a suitable selection of the gain λ_u.

3.1.2. Line-of-sight path following control

As shown in Figs. 1–2, the position of the UGV in NED coordinates can be written as $p = [x_n\ y_n] \in \mathbb{R}^2$ and the corresponding speed is defined as

$$U := \sqrt{\dot{x}_n^2 + \dot{y}_n^2} := \sqrt{u^2 + v^2} \in \mathbb{R}^+. \tag{19}$$

The direction of the velocity vector with respect to the North axis is given by

$$\chi = \tan^{-1}\left(\frac{\dot{y}_n}{\dot{x}_n}\right) \in \mathbb{S} := [-\pi, \pi]. \tag{20}$$

Consider a straight-line path defined by two consecutive waypoints at positions $p_k = [x_k\ y_k]^T \in \mathbb{R}^2$ and $p_{k+1} = [x_{k+1}\ y_{k+1}]^T \in \mathbb{R}^2$, respectively. The path makes an angle of

$$\alpha_k = \tan^{-1}\left(\frac{y_{k+1} - y_k}{x_{k+1} - x_k}\right) \in \mathbb{S} \tag{21}$$

with respect to the North axis of the NED frame. The coordinates of the UGV in the path-fixed reference frame are

$$\epsilon = \begin{bmatrix} s \\ e \end{bmatrix} = R_p^T(\alpha_k)(p - p_k) \tag{22}$$

where R_p^T is the transformation matrix from the inertial to the path-fixed frame given by

$$R_p^T(\alpha_k) := \begin{bmatrix} \cos\alpha_k & \sin\alpha_k \\ -\sin\alpha_k & \cos\alpha_k \end{bmatrix}, \tag{23}$$

□ is the along track distance, and □ is the cross-track error (see Fig. 2).From (22) and (23), the cross track error can be explicitly written as

$$\square = -(\square_{\square} - \square_{\square}) \sin \square_{\square} + (\square_{\square} - \square_{\square}) \cos \square_{\square}. \tag{24}$$

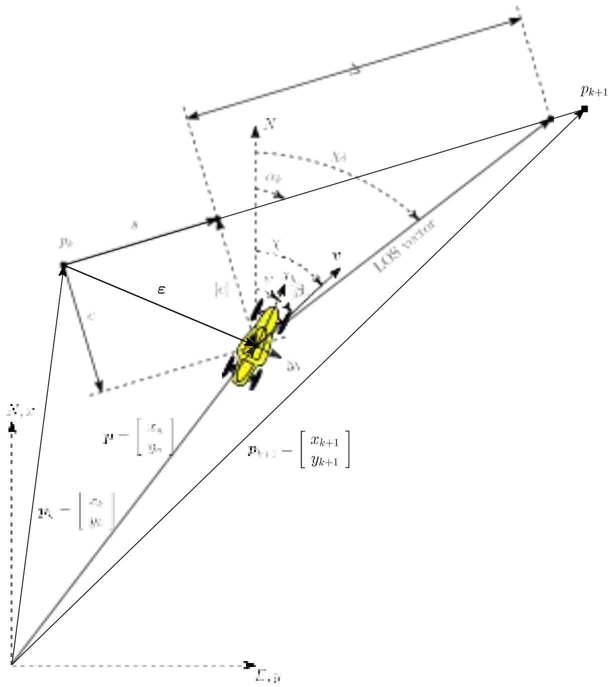

Fig. 2. Line of sight path-following definitions.

Its time derivative, which will be used later, is consequently given by

$$\dot{□} = -\dot{□}_□ \sin □_□ + \dot{□}_□ \cos □_□. \tag{25}$$

From (2) and (3),

$$\begin{aligned} \dot{□}_□ &= □ \cos □ - □ \sin □ \\ \dot{□}_□ &= □ \sin □ + □ \cos □ \end{aligned} \tag{26}$$

so that

$$\dot{□} = -(□ \cos □ - □ \sin □) \sin □_□ + (□ \sin □ + □ \cos □) \cos □_□. \tag{27}$$

Here, the control objectives are formulated to drive the cross-track error to zero by steering the UGV and controlling its forward speed. As mentioned above, the Lookahead-Based Steering Method is used. With this approach a fixed parameter, known as the look-ahead distance □, which corresponds to a distance along the path ahead of the point □, is used to define the LOS vector. The UGV is steered so that its velocity vector is parallel to the LOS vector (Fig. 2). The resulting velocity vector will have a component perpendicular to the path, driving the UGV towards the path until the LOS vector is parallel to the path so that □ → 0.

From Fig. 3 it can be seen that when the velocity vector □ and the LOS vector are aligned, so that □ = , the angles (□$_□$ − □) and □ willbe the same. The change in angle required to achieve this is given by

$$\begin{aligned} □ - □_□ &= -(□_□ - □) + □ \\ &= -(□_□ - □) + \tan^{-1}\left(\frac{□}{□}\right). \end{aligned} \tag{28}$$

Solving for , gives

$$□_□ = □_□ - □ = □_□ + \tan^{-1}\left(-\frac{□}{□}\right). \tag{29}$$

Define the slide-slip angle to be

$$□ = \sin^{-1}\left(\frac{□}{□}\right) \tag{30}$$

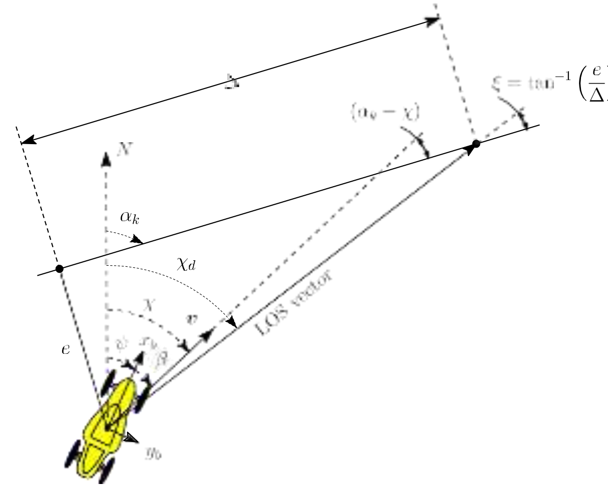

Fig. 3. Relation between , □ and □$_□$.

where □ is the magnitude of the velocity vector □, which can be expressed in the body-fixed reference frame as $□ = \sqrt{□^2 + □^2}$ and in NED reference frame as $□ = \sqrt{\dot{□}^2 + \dot{□}^2}$

For the purposes of control, it is simpler to define the control input in terms of a desired heading angle , instead of the desired course angle □$_□$. From Fig. 3 it can be seen that

$$□ = □ + □ \Rightarrow □_□ = □_□ + □. \tag{31}$$

The desired course angle and desired heading can then be related using (29), as

$$□_□ = □_□ + \tan^{-1}\left(-\frac{□}{□}\right) = □_□ + □, \tag{32}$$

so that

$$□ = □ + \tan^{-1}\left(-\frac{□}{□}\right) - □. \tag{33}$$

Let the heading error be defined as $\tilde{□} := □ - □_□$. Taking the time derivative of the heading error gives

$$\dot{\tilde{□}} = \dot{□} - \dot{□}_□ = \dot{□} - \frac{d}{d□}\left[□_□ + \tan^{-1}\left(-\frac{□}{□}\right) - □\right]. \tag{34}$$

From Fig. 3, we have that

$$\tan □ := \left(\frac{□}{□}\right). \tag{35}$$

By definition,

$$\frac{d}{d□}\tan □ = \frac{1}{\cos^2 □}\dot{□} \tag{36}$$

while

$$\frac{d}{d□}\left(\frac{□}{□}\right) = \frac{\dot{□}}{□}. \tag{37}$$

Thus, using (35) to equate the left hand sides of (36) and (37),

$$\dot{□} = \cos^2 □ \frac{\dot{□}}{□}. \tag{38}$$

From Fig. 3 it can be seen that $\cos □ = □/\sqrt{□^2 + □^2}$. Substituting this expression into (35) above yields

$$\begin{aligned} \frac{d}{d□}\left[\tan^{-1}\left(-\frac{□}{□}\right)\right] &= -\dot{□} \\ &= -\frac{□}{(□ + □^2)}\dot{□} \end{aligned} \tag{39}$$

Thus, the time derivative $\dot{\tilde{□}}$ is

$$\dot{\tilde{□}} = (□ -) + \frac{□}{□_□ + (□^2 + □^2)}\dot{□} + \dot{□},$$

∫40

$$= \sin^{-1} \frac{\square}{\sqrt{\square^2 + \square^2}},$$

where $\tilde{□} := □ - □_□$ is the yaw rate error and $□_□$ is the desired yaw rate. Thus, let

$$□_□ := -\frac{□}{(□^2 + □^2)}\dot{□} - □, \tag{41}$$

be a *virtual control input* such that the heading error dynamics become

$$\tilde{□} = \tilde{□} \tag{42}$$

Next, the definition of the yaw rate error $\tilde{□} := □ - □_□$ and (5)–(9) can be used to rewrite the equation of motion for the yaw rate as

$$□_□\dot{\tilde{□}} = -□_□□_□ + □_□ + □_□. \tag{43}$$

A super-twisting steering controller can be implemented with the control input

$$\begin{aligned} □_{□□} &= \mathrm{sat}_{□_{□\max}}\left(-□_□|□_□|^{1/2}\mathrm{sgn}(□_□) + □_{□1}\right), \\ \dot{□}_{□1} &= \begin{cases} 0, & |□_{□□}| = □_{□\max}, \\ -□_{□1}\mathrm{sgn}(□_□), & |□_{□□}| < □_{□\max}, \end{cases} \end{aligned} \tag{44}$$

where $□_□$ is a sliding surface defined as $□_□ := \tilde{□} + □_□\tilde{□}$, $□_{□\max}$ is the maximum yaw moment that can be generated by the UGV, and $□_□$, $□_□$ and $□_{□1}$ are controller design parameters.

Then, using (41) in (40) and (44) in (43) the closed loop yaw and yaw rate error systems are given by

$$\begin{aligned} \dot{\tilde{□}} &= \tilde{□}, \\ \dot{\tilde{□}} &= -\dot{□}_□ + □_□ + \mathrm{sat}_{□_{□\max}}\left(-□_□|□_□|^{1/2}\mathrm{sgn}(□_□) + □_{□1}\right). \end{aligned} \tag{45}$$

The system (45) can be rewritten as

$$\frac{□_□}{□_□}\dot{□}_□ = □_□ + \mathrm{sat}_{□_{□\max}}\left(-□_□|□_□|^{1/2}\mathrm{sgn}(□_□) + □_{□1}\right), \tag{46}$$

where

$$□_□ = \frac{□_□}{□_□}\tilde{□} - □_□□_□ + □_□. \tag{47}$$

As with the super-twisting speed controller developed in Section 3.1.1 above, the value of $□_{□1}$ will become equivalent to that of $□_{□_□}$ (equivalent control), such that $□_□$ and $\dot{□}_□$ are driven to zero in finite time and the closed loop error system has a stable equilibrium at $\tilde{□} = 0$ and $\tilde{□} = 0$ for a suitable selection of the gains $□_□$, $□_{□1}$ and $□_□$.

3.1.3. Combined machine control input

Using (16) and (44) the total control input from the machine is given by the vector

$$□_□ = \begin{bmatrix} □_{□□} \\ 0 \\ □_{□□} \end{bmatrix}. \tag{48}$$

3.2. Human control

A two-axis force-feedback joystick is used to provide human input. The joystick is configured so that the position of its handle tracks the surge speed and steering control inputs from the automatic controller, i.e. the two components of (48). When moving straight forward at a desired constant speed in the absence of any disturbances, the control inputs from the automatic controller would be $□_{□□} = □_{□0}$ and $□_{□□} = 0$. These values are taken to correspond to the zero position of the joystick, i.e. no displacement along either the front-to-back or side-to-side direction.

By actuating the joystick handle away from its tracked position, a user can signal his/her intent to give the UGV a different speed or steering direction from those commanded by the automatic controller. When this occurs, a force, which is linearly proportional to the angular displacement from the tracked position along each axis, is fedback to the user's hand

$$□_□ = □_□□, \qquad □_□ = □_□□, \tag{49}$$

where $□_□ > 0$ is a spring constant, □ is the displacement from the tracked position along the surge direction, and □ is the displacement from the tracked position along the steering direction. Note that a single stiffness parameter is used to compute the feedback forces so that the human experiences the same stiffness response in both directions.

The surge speed control input from the human is then taken to be

$$□_{□h} = □_{h□}□, \tag{50}$$

where $□_{h□} > 0$ is a constant, and the heading control input from the human is

$$□_{□h} = □_{h□}□, \tag{51}$$

where $□_{h□} > 0$ is a constant.

Then, using (50) and (51), the total control input from the human is given by the vector

$$□_h = \begin{bmatrix} □_{□h} \\ 0 \\ □_{□h} \end{bmatrix}. \tag{52}$$

Assumption 3. As is often done in the analysis of teleoperated systems [24], the system is assumed to be passive. In general, this can be mathematically expressed as

$$\int_0^□ \left(□_h\dot{□}_{1h} - □_□\dot{□}_1\right) d□ \geq 0, \tag{53}$$

where $□_h$ is the force applied by a human, $□_□$ is an external force applied by the environment, $\dot{□}_{1h}$ is the speed at which the teleoperated system is being displaced (e.g. the handle of a joystick) and $\dot{□}_1$ is the speed at which the controlled system is moving. Here, since the system is not manipulating its environment, no external forces act on the system (apart from disturbances, which are assumed to require minimal human input to counteract), so that (53) becomes

$$\int_0^□ □_h\dot{□}_{1h} d□ \geq 0 \tag{54}$$

and the human input alone is passive.

Measures of a human's intent to the control the speed $□_{h□}$ and direction $□_{h□}$ of the system can be defined using Assumption 3. Let $\dot{□}$ and $\dot{□}$ be the rates at which the joystick handle is being moved away from the tracked position. Then, using (49) in (54), the measures become

$$□_{h□} := \int_0^□ □_□\dot{□}d□ = \int_0^□ □_□□\frac{d□}{d□}d□ = \frac{1}{2}□_□□^2 \geq 0 \tag{55}$$

and

$$□_{h□} := \int_0^□ □_□\dot{□}d□ = \int_0^□ □_□□\frac{d□}{d□}d□ = \frac{1}{2}□_□□^2 \geq 0. \tag{56}$$

Note that $□_{h□} > 0$ and $□_{h□} > 0$ whenever the joystick handle is displaced from the tracked position in either the front-to-back $□ \neq 0$ or side-to-side directions $□ \neq 0$, and $□_{h□} = 0$ and $□_{h□} = 0$ only when $□ = 0$ or $□ = 0$, making it a convenient measure of the human's intent to control the system.

3.3. Control input blending

A mixed-initiative approach is used where, as mentioned above, $□_{h□}$ and $□_{h□}$ are used as a measure of the human's intent to control the plant. In a fashion similar to (1), a pair of arbitration matrices are defined as

$$□_h := \begin{bmatrix} (1 - e^{-□_h}) & 0 & 0 \\ 0 & 0 & 0 \\ 0 & 0 & (1 - e^{-□_h}) \end{bmatrix} \tag{57}$$

and

$$□_□ := \begin{bmatrix} e^{-□_{h□}} & 0 & 0 \\ 0 & 0 & 0 \end{bmatrix}$$

0 0 $e^{-\square h \square}$ $\Big]$, (58)

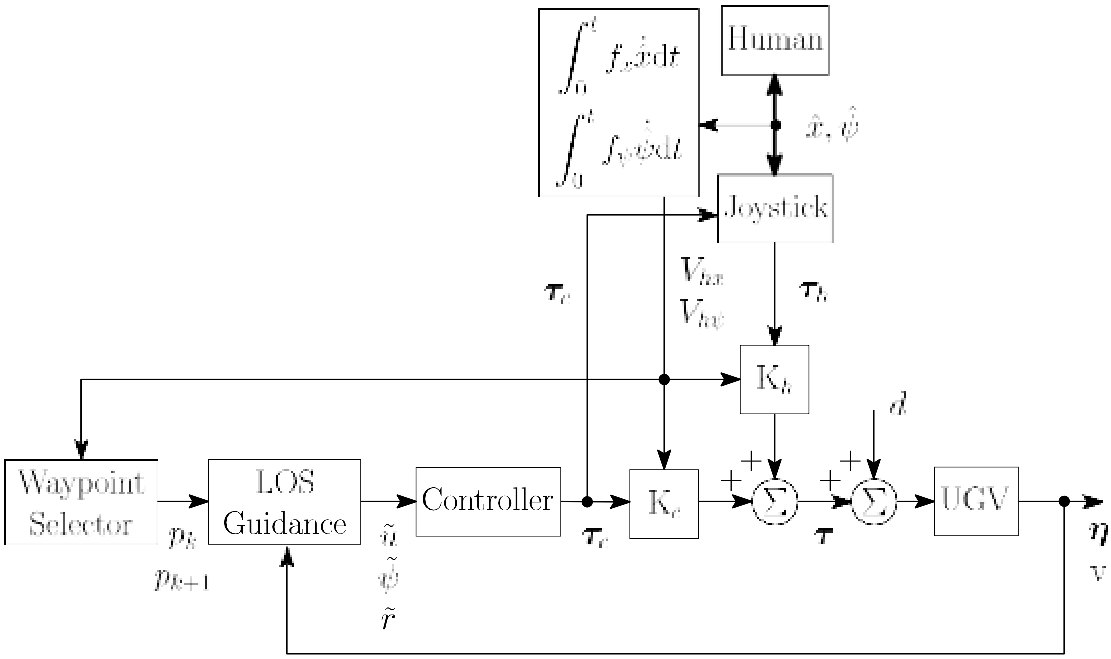

Fig. 4. Block diagram of the shared control system.

where $K_h + K_c = I$. Then, the blending is performed as

$$\tau = K_h \tau_h + K_c \tau_c . \tag{59}$$

so that as V_{hx} and $V_{h\psi}$ increase, the elements of K_c decrease and the level of automatic control is reduced in favor of human input. A block diagram of the overall system is given in Fig. 4.

3.4. Stability of the shared control system

A stability proof of the shared human–machine control system can be decomposed into three main parts:

(1) the stability of the human-controlled system;
(2) the stability of the closed loop machine control system; and
(3) a demonstration that the combined control input cannot exceed the actuator magnitude limits.

Firstly, under Assumption 3, the human component of the system is assumed to be passive, i.e. the human does not intentionally drive the system errors to infinity.

Turning to the stability of the super-twisting controllers, it can be seen from Eqs. (17) and (46) that the closed loop dynamics of both the surge speed error and the yaw rate error have the form

$$\dot{\sigma} = u_\sigma + \varphi , \tag{60}$$

where the state σ can be either $\tilde{u}$ or s_ψ, u_σ is the corresponding control input (either the τ_{cx} or $\tau_{c\psi}$), and φ_σ is the corresponding perturbation (either φ_u or φ_ψ). In keeping with Assumption 1 the perturbations are assumed to be bounded $|\varphi_\sigma| \leq \Phi$ and composed of two components, $\varphi_\sigma = \varphi_{\sigma 1} + \varphi_{\sigma 2}$, where $\varphi_{\sigma 1}$ is Hölder continuous in the state and $\varphi_{\sigma 2}$ is Lipschitz continuous in time, such that

$$|\varphi_{\sigma 1}| \leq \delta_\sigma |\sigma|^{\frac{1}{2}}, \quad |\dot{\varphi}_{\sigma 2}| \leq \Delta_\sigma , \tag{61}$$

where δ_σ, Δ_σ and Φ_σ are non-negative constants. The control input is bounded by a positive constant $U_{\max}$, i.e. $|u_\sigma| \leq U_{\max}$, where it is assumed that $U_{\max} > \Phi_\sigma$ in order to for the control task to be feasible.

The finite time stability of the saturated super twisting controller is proven in [36].

Theorem 1 (*After [36]*). *Consider the system (60) and the saturated super-twisting control input*

$$u_\sigma = \mathrm{sat}_{U_{\max}}\left(-k_1 |\sigma|^{\frac{1}{2}} \mathrm{sgn}(\sigma) + u_{\sigma 1} \right), \tag{62}$$

$$\dot{u}_{\sigma 1} = \begin{cases} 0, & |u_\sigma| = U_{\max}, \\ -k_2 \mathrm{sgn}(\sigma), & |u_\sigma| < U_{\max}, \end{cases}$$

where $k_1 > 0$ and $k_2 > 0$ are control gains, and $u_{\sigma 1}(0) = 0$.

If

$$\begin{aligned} k_1 &> \delta_\sigma + \sqrt{2\Delta_\sigma + 2k_2}, \\ k_1 &> \frac{\delta_\sigma}{2} + \sqrt{\frac{\delta_\sigma^2}{4} + 2\,\frac{U_{\max} + \Phi_\sigma}{U_{\max} - \Phi_\sigma}}, \\ k_2 &> \Delta_\sigma , \end{aligned} \tag{63}$$

the closed loop system is globally finite time stable, and the control input u_σ is continuous and satisfies the actuator magnitude constraint $|u_\sigma| \leq U_{\max}$.

The proof of Theorem 1 in [36] is based on the construction of an invariant set for which the control input can neither exceed, nor slide along the saturation limit $|u|_\sigma = U_{\max}$. A composite Lyapunov function is designed using multiple Lyapunov functions to make the state bound arising from the saturation limits coincide with the level set of one of its component Lyapunov functions in a certain region of the state space. This guarantees that u_σ satisfies the control input bound (in the region of the state space that the state bound is defined), but still uses a *traditional* elliptic Lyapunov function in the region of the state space where the saturation limit does not impose a state bound. The approach guarantees disturbance rejection using a continuous control signal. The interested reader is encouraged to see the complete proof in [36], and the related paper [37], for additional details.

Since the super-twisting controllers drive both the speed error $\tilde{u}$ and the sliding surface s_ψ to zero in finite time, from (45) it can be seen that both the yaw angle error $\tilde{\psi}$ and the yaw rate error $\tilde{r}$ are also driven to zero in finite time. Thus, the finite time stability of the closed loop path following controller with actuator magnitude constraints, model uncertainty, and in the presence of bounded disturbances, is guaranteed.

Lastly, we show that the combined control inputs from the human and the automatic controller cannot exceed the actuator magnitude limits.

Table 2
Main particulars of the model dune buggy.

Parameter	Value
Car length □	844×10^{-3} [m]
Car width □	501×10^{-3} [m]
Car height □	308×10^{-3} [m]
Wheelbase WB	552×10^{-3} [m]
Distance center mass to front axle	292×10^{-3} [m]
Distance center mass to rear axle	260×10^{-3} [m]
Car mass □	13.8 [kg]
Car mass moment of inertia □□ (about □□ axis)	1.12 [kg-m^2]

Theorem 2. *Let the shared control input □□ along channel □ (where □ could be either □ for the surge speed control input or □ for the heading control input) be composed of a human input $□_{h□}$ and a machine control input □□□. If the magnitudes of both $□_{h□}$ and □□□ are upper bounded by the same positive constant, i.e.* |□ | ≤ □ $_{max}$ *and* |□ | ≤ □ $_{max}$, *then for a given value of the storage function $□_{h□} \geq 0$ the shared control input governed by the blending rule* (59) *and the convex exponential function pairs given by the arbitration matrices* (57) and (58) *is also upper bounded by* □□ ≤ $□_{□max}$.

Proof. For a given value of □| | ≥ 0, □ ≤ □ $_{max}$e$^{-|□h□}$ and □ ≤ $□_{□max}$(1 − e$^{-□h□}$). By the Triangle Inequality |□□□ + $□_{h□}$| ≤ |□□□| + |$□_{h□}$|. Therefore,

$$|□_{□□} + □_{h□}| \leq □_{□max} e^{-□h} + □_{max} (1 - e^{-□h})$$
$$\leq □_{□max}. \quad \square$$

4. Methods

A series of experiments was conducted using a small UGV configured to semi-automatically follow a lawn mower shaped search pattern. With no human input, the onboard controller on the UGV enables it to automatically follow the path. Using a force reflexive joystick, a human user can either take full manual control of the vehicle by continuously actuating the joystick (tight rein), or rely on semi-automatic (loose rein) control in one of two ways: (a) a user can briefly actuate the joystick to make the UGV deviate slightly from the path, for example to avoid an obstacle and then automatically return to the path, or (b) by actuating the joystick longer and then releasing it, a user can trigger an automatic switch to the next leg of the lawn mower search path. Three test cases are studied: (1) loose rein shared control with only temporary deviations from a preplanned path (no lane changes), (2) loose rein control with lane changing, and (3) tight rein shared control. With shared human–robot control the system operates semi-automatically (to permit the human to focus on higher level tasks, etc. while still having some input, when needed). Thus, the experiments are designed so that the UGV proceeds along the survey path at an almost constant speed (under mainly closed loop automatic speed control), with most of the human input related to steering the UGV, for example to get closer look at an object of interest away from the path, or to avoid an obstacle. The details of the experimental configuration and test setup are provided in this section.

4.1. Experimental setup

A schematic overview of the experimental setup is provided in Fig. 5. A four wheel drive Losi Desert Buggy XL-E 1/5th-scale model electric dune buggy was modified for use as a robotic test platform (Fig. 6). The vehicle is produced by Horizon Hobby of Champaign, Illinois, USA. The main parameters are provided in Table 2.

A laptop computer was used as a ground station to monitor and supervise the progress of experiments, which is indicated as the guidance navigation and control (GNC) Groundstation Computer block in Fig. 5. The Mission Planner ground station graphical user interface (GUI) was

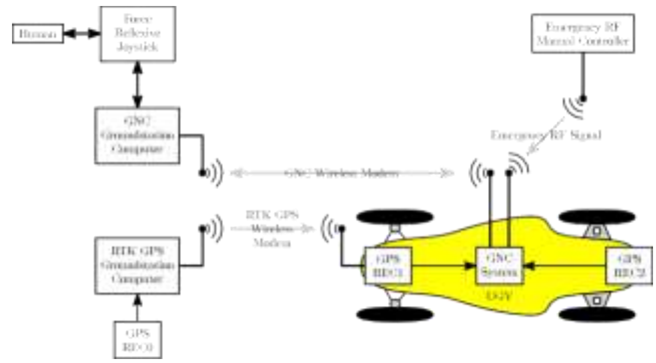

Fig. 5. Experimental Configuration. REC is an abbreviation for the word receiver; the remaining acronyms are defined in the main text.

used to permit a user to see the vehicle status, construct and upload the

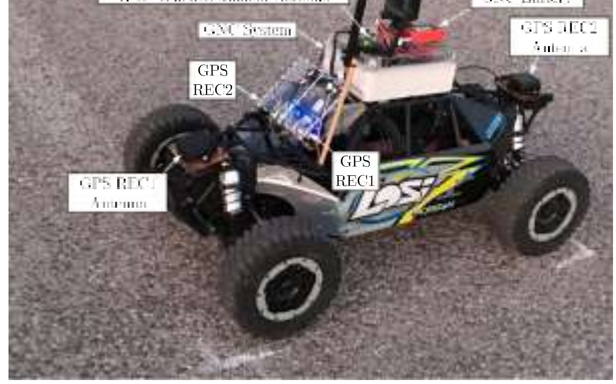

Fig. 6. The unmanned ground vehicle. The GNC system box includes the PixHawk microcontroller, a voltage regulator, and an RF receiver. The GNC system battery is mounted externally so that it can be quickly changed.

desired waypoints for the vehicle to follow, set/tune controller gains, observe the progress of the mission and interrupt or alter the missionin real time [38].

A radio frequency (RF) modem is used for two-way communication between the ground station and vehicle (the GNC Wireless Modem signal in Fig. 5). Specifically, vehicle telemetry, including pose andspeed, is transmitted to the ground station and the human joystick inputis relayed to the vehicle controller. Vehicle state information is logged and displayed in real-time on a graphical user interface (GUI). With theuse of a hand-held remote control unit, it is also possible for a user to override onboard computer control of the vehicle and manually steerit in case of an emergency (the Emergency RF Manual Controller block and signal in Fig. 5).

The force reflexive joystick used is a CLS-P Sidestick Active Force Feedback Joystick, produced by Brunner Elektronik AG of Hittnau, Switzerland. The joystick, which resembles the control stick of an Airbus A320 passenger airplane, has two degrees of freedom, i.e. pitch androll. The output of the pitch channel is used as the human throttle inputsignal, while the roll channel is taken as the human steering input.Both axes are equipped with load cells for torque measurements and optical encoders for position feedback. The most relevant propertiesof the device are listed in Table 3. Software was written in-house to read the joystick inputs and to convert them into messages that can be passed to the UGV using wireless telemetry (indicated as the GNC wireless model in Fig. 5). The custom joystick software was also used to linearly scale the speed and cross track errors, which are transmitted from the UGV to the ground station as part of the vehicle telemetry

Table 3
Main properties of the force-feedback joystick.

Parameter	Value
Maximum travel (pitch/roll)	±20°
Magnitude peak torque (pitch/roll)	50 [N-m]
Position accuracy (pitch/roll)	±2%
Torque accuracy (pitch/roll)	±2%

data, into forces, that are fedback to the user through the force reflexive joystick.

The PixHawk Cube 2.1 autopilot system manufactured by Hex Aero of Hong Kong, China is employed for GNC and is indicated as the block labeled GNC System in Fig. 5. The system includes an integrated attitude and heading reference system (e.g. inertial measurement unit, accelerometers, rate gyros and a magnetometer). The system also has several input–output ports for PWM control of servo motors, general purpose serial ports and a CAN bus interface. Additional details of both the hardware and software architecture of the autopilot can be found in the work of [39].

The speed and path following controllers presented in Section 3.1 and blending of the human and machine control inputs signals, as described in Section 3.3, were implemented by modifying existing open source ArduPilot software [40] and then installing it as firmware on the autopilot system using the Mission Planner ground station software application [38].

The vehicle's position, speed and heading are measured using a pair of simpleRTK2B real-time kinematic (RTK) GPS systems, which are produced by Ardusimple of Lleida, Spain. GPS receivers are placed along the centerline of the vehicle with a baseline (separation) distance of 74 cm. The system exploits the relative positions between a GPS receiver placed at the front of the UGV and a second GPS receiver located at the rear of the vehicle to compute heading (see blocks GPS REC1 and GPS REC2 in Fig. 5). This heading measurement is more accurate than the measurement provided by the magnetometers resident on the autopilot system. The calculations required for these heading measurements are included in the custom-written autopilot software discussed above. RTK GPS systems use a radio frequency signal transmitted from a fixed base station to provide a more accurate positioning measurement. The RTK receiver base station was implemented using a second computer, as shown in Fig. 5.

4.2. Lawn mower pattern shaped search path

The path followed by the UGV is designed to represent a lawn mower pattern shaped search path commonly used for environmental measurement or mapping applications that employ unmanned vehicles. The path consists of five 37.5 m long segments joined together by shorter 5 m segments (Fig. 7). The tests are conducted in a small portion of the parking lot outside a ranchers' market. The ground crossed by the path is partially paved, partially covered by grass and gently slopes downward in the North-to-South direction. It also contains several small holes, a low-lying drain, and small debris, including rocks, sticks and even apples. While the effects of the uneven ground and debris are difficult to quantify, they provide a natural source of exogenous disturbances.

4.3. Lane changes

With no human input the UGV automatically follows the path, moving past each waypoint in sequential order, until traversing the entire path one time in each direction (Fig. 7).

When the human actuates the joystick, the total control input contains a human component and a machine component, i.e. the control input is shared by the human and machine. As discussed at the beginning of Section 4, the shared control can be categorized as being either

Fig. 7. Waypoint defined paths. Waypoints are indicated with numbered green symbols, the paths are outlined with yellow lines. The radius of acceptance $\square_{\square}$ around each waypoint is indicated by a dashed white circle. The orange and white object in the upper left hand corner is a front loader. (For interpretation of the references to color in this figure legend, the reader is referred to the web version of this article.)

loose rein or tight rein. There are two types of loose rein behavior, which are determined by the value of $\square_h$. When $\square_{h\square}$ is below a threshold value $\square_h < \square_{h\square\square}$, the vehicle continues to sequentially follow the waypoints. The force reflexive joystick applies a force against the user's hand, which is proportional to the cross track error in along the roll axis of the joystick and the speed error along the pitch axis of the joystick to signal that the user is commanding the vehicle to deviate from the preplanned path and/or speed. This type of shared control can be useful for situations in which a user wants to temporarily deviate from the path in order to avoid an obstacle that the UGV's perception system does not correctly identify, or to slow down slightly to permit a remote user to have a longer look at something via an onboard camera,for example.

If the human actuates the joystick for longer, or more vigorously, such that $\square_{h\square} \geq \square_{h\square\square}$, a lane changing system is triggered when the UGV is on one of the longer (37.5 m) path segments. If the UGV is on an outer leg of the path and the user actuates the joystick to steer the UGVtowards one of the inner legs of the path, or if the UGV is already within the inner legs of the path when the user first actuates the joystick, the system will switch to the next parallel path segment, also switching the planned direction of travel along the new path segment (so that the UGV does not need to turn around to continue following the planned path), see Fig. 8. In this mode the user can continue to actuate the joystick and the lane changing system will continue switching across legs of the path until the user releases the joystick.

If the UGV is on one of the outer legs of the path and the user moves away from the path, the system permits the user to manually drive the UGV. In this situation, the user can manually drive the UGV away from the lawn mower search pattern to explore areas off of the preplanned path. The forces applied to the human's hand by the force reflexive joystick are magnitude constrained, so when the user is

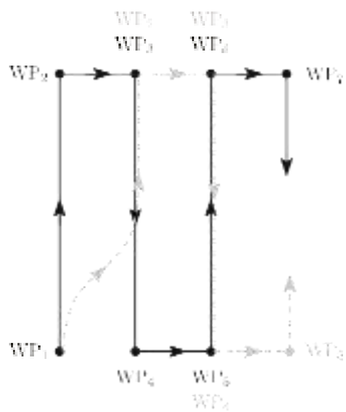

Fig. 8. An example of a lane change. If a lane change is not triggered, the UGV follows the preplanned path (solid black line segments and text), moving past each waypoint in sequential order along the directions indicated. When a lane change is triggered, the UGV transits to the neighboring leg of the path, dropping two waypoints and changing the direction along the preplanned lengthwise legs of the path, as indicated by the dashed gray lines and text.

Table 4
Parameter values used in the experiments.

Parameter	Value	Description
□	1.5	Look-ahead distance [m]
$\square_{\square}$	2.5	Circle of acceptance radius [m]
$\square_{\square}$	0.075	Speed controller low order gain
$\square_{\square 1}$	0.125	Speed controller high order gain
$\square_{\square max}$	100.0	Max. surge speed throttle input [%]
$\square_{\square}$	1.0	Heading controller yaw rate gain
$\square_{\square}$	0.1	Heading controller low order gain
$\square_{\square 1}$	0.2	Heading controller high order gain
$\square_{\square max}$	20.0	Max. heading control input [deg]
$\square_{\square}$	1.0	Joystick spring constant
$\square_{h\square}$	100.0	Human input speed control gain
$\square_{h\square}$	20.0	Human input heading control gain
$\square_{h\square\square}$	0.45	Threshold $_{h\square}$ to trigger lane change

driving off of the lawn mower search grid, the joystick applies forces pulling the user back towards the search grid, but these forces are no longer proportional to the cross track, and speed, errors.

4.4. Experimental parameter settings

Table 4 contains a list of the important parameters used in the experiments. The settings were first selected by performing simulations using the Ardupilot software-in-the-loop simulator and manually tuning to achieve good performance. Once the simulated performance was acceptable, the system was implemented experimentally and additional manual tuning was performed in the field.

During the simulation tuning stage, common rules of thumb were used to select the initial values of the parameters used. For example, the lookahead distance □ for path following is usually about 1.5□ to 2.5□, where □ is the length of the vehicle [31]. Longer lookahead distances provide a smoother, but slower, convergence to the desired path. The value of the waypoint circle of acceptance $\square_{\square}$ was selected by how closely we wanted the vehicle to approach the waypoints at each corner, considering that traversing from a long leg of the search path to a shorter leg of the search path requires a fairly tight turn at speed.

The gains of the super twisting controllers were tuned by examining the time history of the first and second order terms in simulation. The second order terms tend to display an effect similar to windup when the gain of the second order term is too high. The gains of the second order terms were tuned until the windup like effect was eliminated. We then selected the first order gains by trial and error to achieve satisfactory speed and steering performance. Minimal additional tuning of the controller parameters was required when they were implemented on the physical platform. Specifically, the surge speed controller gains $\square_{\square}$ and $\square_{\square 1}$ were increased slightly to make the UGV accelerate faster.

To determine the human control inputs, the measured displacements of the joystick from its tracked position are first mapped to the ranges $-1 \leq \hat{\square} \leq +1$ and $0 \leq \hat{\square} \leq +1$ and then scaled by the human input surge speed control gain $\square_{h\square}$ and the human input heading control gain $\square_{h\square}$, respectively, so that the maximum steering angle commanded by the user is ±20° and the maximum throttle is +100% (the commanded throttle is always greater than or equal to zero, as we did not want the UGV to have the capability of reversing).

The threshold value of $\square_{h\square}$ for triggering lane changes, $\square_{h\square\square}$, was determined via experimentation. By trial and error, the value was selected to be large enough to avoid unwanted lane changes, but low enough that lane changes could be fairly easily triggered by the human, when desired.

Lastly, the spring constant of the joystick was selected as $\square_{\square} = 1$ by trial and error.

As the UGV is operated at low speeds during all of the experiments, the side slip angle □ in (33) and its time derivative $\dot{\square}$ in (41) were taken to be zero for simplicity.

Note that the theoretically derived control inputs are the surge force $\square_{\square}$ (e.g. in [N]) and the yaw moment $\square_{\square}$ (e.g. in [N-m]), see (9). However, it is not possible to command a specific force and torque from the physical platform. As mentioned in Section 4.1, a PixHawk Cube autopilot is used to control the UGV. The steering input to the PixHawk is given in degrees and the forward speed is commanded as a percentage of throttle. Therefore, in implementation the shared control inputs $\square_{\square}$ and $\square_{\square}$ in (9) are constructed as shown in (59) and directly inserted into the throttle command (in percent) and the steering command (as an angle in degrees), respectively. As explained above, the controller gains are tuned to ensure the control inputs are within the correct input ranges of the throttle and steering actuators, and the corresponding actuator magnitude limits are also explicitly set to $\square_{\square max} = 100\%$ and $\square_{\square max} = 20°$ to ensure that the controller respects the limits of the physical actuators (see Table 4). While related, the actuator limits of the drive motor (in percentage of throttle) and the steering angle of the front wheels (in degrees) do not have a one-to-one correspondence to the theoretically defined surge force limit (e.g. in [N]) and yaw moment limit (e.g. in [N-m]). However, according to the theory, as long as the actuator limits correspond to surge forces and yaw moments larger than the corresponding anticipated disturbances, the closed loop system will be stable (see Section 3.4).

5. Results & discussion

Representative results from the three test cases introduced at the beginning of Section 4 are shown in Figs. 9–13. In these figures, the experimentally-measured location of the UGV is expressed as an □ − □ position in meters from the first waypoint in the lawn mower pattern shaped search grid. The grid itself is indicated in the UGV position plots as a set of dashed gray lines. The color of the UGV position data points is used to provide a sense of when the human is trying to control the UGV. When the human input measured by the joystick is low, the position measurements are black. When the joystick is strongly actuated by the human along the pitch axis of the joystick (steering direction), the position measurements are red, when forcefully actuated along the pitch axis of the joystick (speed direction), the position measurements are blue, when both axes are forcefully actuated, the position measurements are colored purple. The numbers next to the position measurements indicate the time in seconds since the start of the experimental run and provide a means of correlating the position measurements and their associated time series measurements.

As can be seen in the steering angle data presented in Fig. 9b, there is a time delay between the automatic control input and the joystick signal, which contains the human input. Using a cross correlation

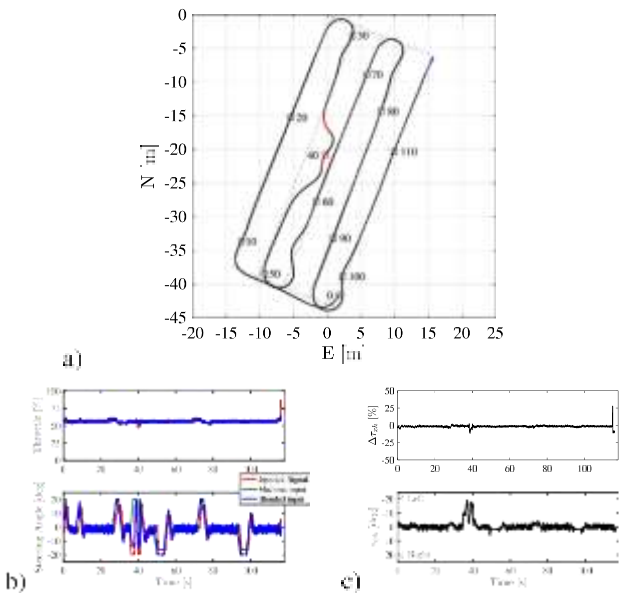

Fig. 9. Loose rein without lane changing: (a) position measurements; (b) throttle and steering commands; (c) approximate human input (□□$_{h□}$ corresponds to the human throttle input relative to the input from the automatic controller).

analysis of the two signals, the time delay is found to be □$_□$ = 0.98 s. The delay is caused by the limited bandwidth of the radio modem used for communication between the UGV and ground station. The data transmitted include navigation information, joystick commands, UGV status and automatic control system information. Several attempts were made to reduce the time delay by minimizing the quantity of the data transmitted. However, a time delay of = 0.98 s was the minimum the authors were able to obtain.

Estimates of the human throttle and steering inputs to the joystick (Figs. 9b, 11b and 13b) were obtained by: (1) shifting the joystick signals backward in time, e.g. let $\bar{□}_{js}$(□) = □$_{js}$(□ + □$_□$) and $\bar{□}_{js}$(□) = □$_{js}$(□ + □$_□$) be the shifted signals along the pitch and roll axis of the joystick, respectively, where $\bar{□}_{js}$ and $\bar{□}_{js}$ are the shifted signals and □$_{js}$ and □$_{js}$ are the original signals; (2) zero-padding $\bar{□}_{js}$ and $\bar{□}_{js}$ for times □$_□$ −□$_□$ ≤ □ ≤ □$_□$, where □$_□$ is the time at the end of the run (i.e. the time at which the measurements were stopped); and (3) computing ($\bar{□}_{js}$ − □$_{□□}$)∕2 and ($\bar{□}_{js}$ − □$_{□□}$)∕2 to obtain the human throttle and steering control inputs, respectively. The resulting data are shown in Figs. 9c, 11c and 13c, where the human throttle and steering inputs can be correlated with the associated position data seen in Figs. 9a, 11a and 13a.

The loose rein without lane changing case is demonstrated in Fig. 9. In the experiment shown, the lane changing system is not enabled. The UGV is permitted to follow the path under automatic (machine) control, apart from a brief intervention by the human at times of approximately 37 ≤ □ ≤ 42 s. During this time interval, the human actuates the steering axis of the joystick causing the UGV to temporarily turn to its left. When the joystick is released and not further actuated, the UGV follows the original path.

It was not possible to quantitatively validate the robustness of the automatic controller via experiment, e.g. by imposing known (measured) external forces/moments on the UGV and measuring the subsequent path following error responses. However, as noted in Section 4.2, the test site is located in an area with uneven ground and a substantial amount of small debris, which effectively introduce unknown exogenous disturbances on the system. Despite the disturbances introduced by the environment, the second order sliding mode based automatic control system follows the path well, as can be qualitatively seen by comparing the measured UGV position and the preplanned path lines

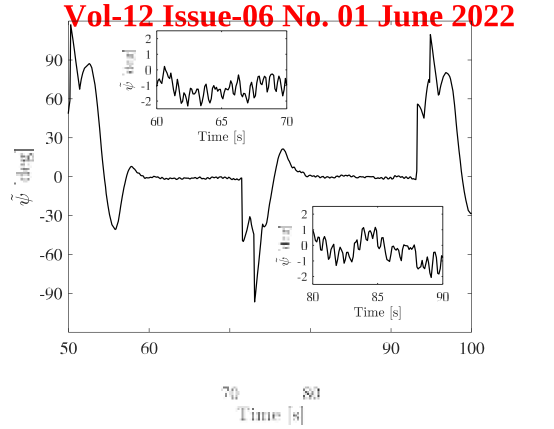

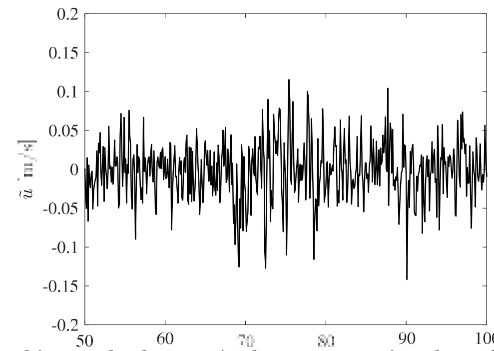

in Fig. 9a. This can also be seen in the representative plots of heading b)

c)

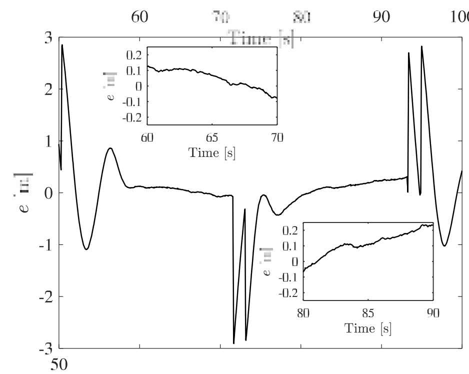

Fig. 10. (a) Heading error ̃□, (b) speed error ̃□ and (c) cross track error □ of the closed loop path following system for times 50 ≤ □ ≤ 100 s, when the system is under automatic control during the loose rein experiments.

error and speed error for the loose rein case shown in Fig. 10 below. The plots show times 50 ≤ □ ≤ 100 s of the loose rein case when there is no human input. At each corner, the heading error ̃□ jumps by about ±90°, but is rapidly driven to near zero by the controller. Along the straight sections of the search path it can be seen from the inset plots in Fig. 10 that the heading error is only about ±2°. Similarly, it can be seen that the speed error □̃ is less than about ±7.5% of the desired speed of □ = 2.0 m/s. Lastly, it can be seen that the cross track error is less than about ±0.2 m for these times, which is small compared to the 5 m × 40 m legs of the search path.

Figs. 11–14 demonstrate the loose rein with lane changing and the tight rein cases. In both cases, the lane changing capability of the UGV is enabled. By comparing Fig. 11 with Fig. 12, and Fig. 13 with Fig. 14, it can be seen that when 0 < $□_{h□}$ < $□_{h□□}$, the vehicle can be moved from the preplanned path slightly (see times 20 ≤ □ ≤ 30 s in Figs. 11–12). However, when $□_{h□}$ ≥ $□_{h□□}$ lane changes are triggered. Multiple lane changes can also be commanded if the human continues to actuate the joystick after a single lane change is achieved (see the time intervals

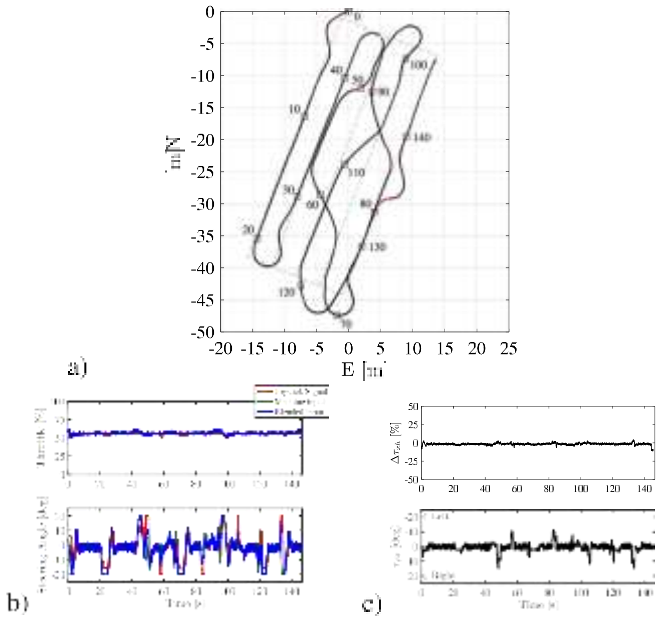

Fig. 11. Loose rein with lane changing: (a) position measurements; (b) throttle and steering commands; (c) approximate human input ($\Delta\tau_{th}$ corresponds to the human throttle input relative to the input from the automatic controller).

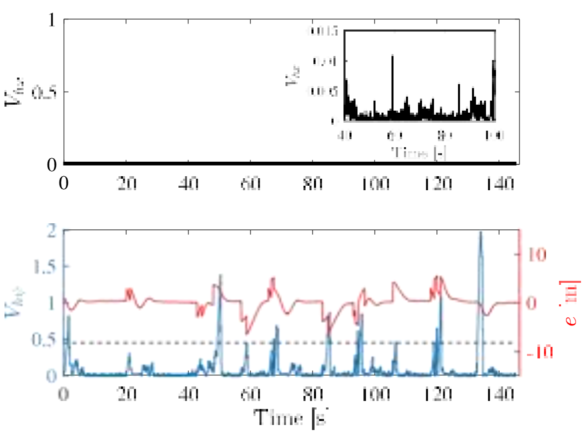

Fig. 12. Loose rein with lane changing: V_{hx} and V_{hy}. The threshold value of V_{hy} that triggers a lane change is V_{hy} = 0.45 and is indicated as a dashed line. Each time a lane change occurs there is a large change in the associated cross track error e. The smallerdouble peaks in e correspond to the corners, where the current and next waypoint are updated. From the inset in the plot of V_{hx}, it can be seen that the human does not actuate the joystick in the x direction to control the speed.

from roughly 55 ≤ t ≤ 65 s and from 80 ≤ t ≤ 90 s in Figs. 11–12, for example).

The tight rein case is illustrated in Figs. 13–14. As mentioned above, when the UGV is on an outer leg of the path, the human can freely drive the UGV when actuating the joystick to move the vehicle away from the path. In Fig. 13 it can be seen that this was done three times during the experiment, approximately corresponding to the time intervals 10 ≤ t ≤ 30 s, 90 ≤ t ≤ 115 s and 130 ≤ t ≤ 145 s. The test site is bounded on both sides by buildings, the walls of which are parallel to the longer legs of the path. During this run, the human actuated the joystick to drive the UGV near the walls of these buildings, as if to better explore the environment in these areas. When the human releases the joystick, the UGV returns to the leg of the path from which it departed, despite the large human-imposed deviations.

From the blended input signals shown in Fig. 11b and Fig. 13b, it

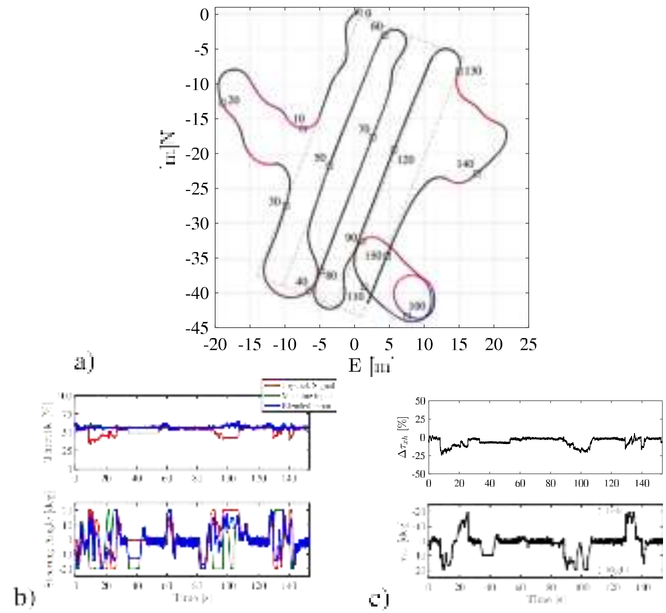

Fig. 13. Tight rein: (a) position measurements; (b) throttle and steering commands; (c) approximate human input ($\Delta\tau_{th}$ corresponds to the human throttle input relative to the input from the automatic controller).

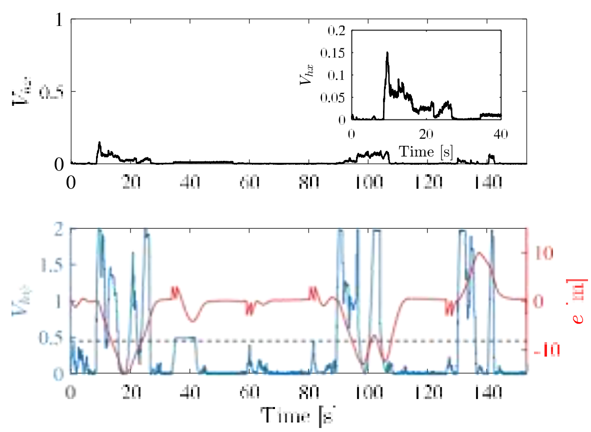

can be seen that the human input has almost no affect on the surge

Fig. 14. Tight rein: $\square_{h\square}$ and $\square_{h}$. The threshold value of $\square_{h\square}$ that triggers a lane change is $_{h\square\square}$ = 0.45 and is indicated as a dashed line. Each time a lane change occurs there is a large change in the associated cross track error □. The smaller double peaks in □ correspond to the corners, where the current and next waypoint are updated. While the human actuates the joystick in the □ direction, $\square_{h\square}$ remains small and the surge speed is not appreciably affected.

speed of the UGV in the loose rein with lane changing and tight rein experiments. As can be seen from the corresponding plots of $\square_{h\square}$ in Figs. 12 and 14 the reason for this is that $\square_{h\square}$ is small throughout the experiments, so that most of the blended input comes from the automatic controller. As pointed out in Section 4.4, the selection of $\square_{\square}$ affects the rates at which the human and the machine control inputs are blended. As the LOS Path Following Algorithm assumes a constant forward surge speed, the value used for the experiments was partially selected based on the fact that it permits the human to mainly focus on steering, while the automatic controller handles the speed. However, as can be seen in Figs. 15–17, which demonstrate another tight rein experiment, it can be seen that when the joystick is vigorously actuated along its □ˆ axis, the user can also control the speed of the UGV. In the experiment shown, the user has driven the UGV off of the survey grid, first commanded a large increase in throttle causing the vehicle to speed up to about 4 m/s, and then pulled back on the throttle

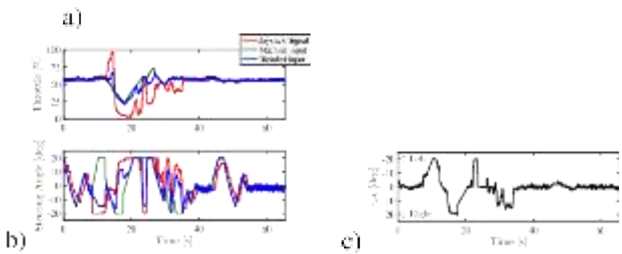

Fig. 15. Tight rein with human speed control: (a) position measurements; (b) throttle and steering commands; (c) approximate human input (□□$_h$□ corresponds to the human throttle input relative to the input from the automatic controller).

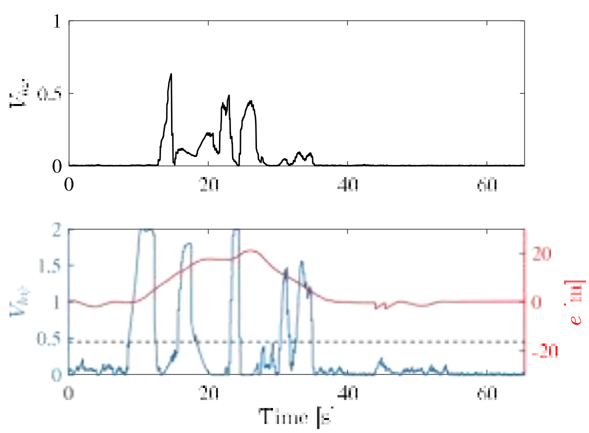

Fig. 16. Tight rein with human speed control: □$_h$□ and □$_h$. The threshold value of □$_h$□ that triggers a lane change is □$_h$□ = 0.45 and is indicated as a dashed line.

to command the UGV to stop for several seconds, before permitting the automatic controller to resume speed control at the normal path following surge speed of 2 m/s.

6. Concluding remarks

Here, an approach for the path-following shared control of an unmanned ground vehicle has been experimentally demonstrated. The behavior of the system adheres to the H-Metaphor shared control concept. The main features of the approach include: (1) super-twisting slide mode controllers for both steering and speed control, which effectively permit the mitigation of exogenous disturbances and model uncertainty via *equivalent control* and the passive measure of human intent to be based solely on the human input; and (2) a mixed-interaction approach for blending the control inputs from the human and the machine via an exponential function (for fast switching), which takes the passive measure of the human input as its argument. The UGV is able to return to its preplanned path, despite large, human-driven excursions. Of special significance is that the human and the machine are not collocated. This introduces additional challenges, such as providing

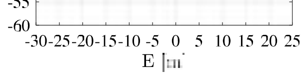

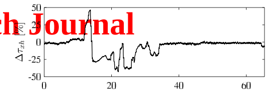

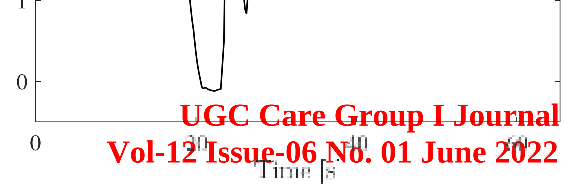

Fig. 17. Tight rein with human speed control: Variation of the surge speed when the human first briefly commands a large increase in throttle, then suddenly pulls back onthe joystick to stop the UGV, and then releases the joystick along the axis so that the automatic controller resumes the normal path following speed of 2 m/s.

the human with adequate situational awareness and ensuring that communication delays do not cause instability.

In future work the authors plan to address includes how to account for communication delays in the control system design, defining metricsto characterize the performance of the shared control system, and how to implement reactive behaviors in the machine control input.

As the main focus of this work is shared human–robot path fol- lowing control, path planning is treated as a separate problem. The waypoints used in the experiments were manually selected to forcethe vehicle to cross multiple types of terrain, various ground slopesand to experimentally demonstrate that the system can robustly fol- low a desired path both across long distances and with sharp turns. Another very interesting area of further study could be to explore how the process of waypoint selection could be accomplished by using a path planner with shared control human-in-the-loop simulations beforedeploying the physical system so that the resulting path is well-suitedto the human–machine system.

CRediT authorship contribution statement

Karl D. von Ellenrieder: Conceptualization, Methodology, For- mal analysis, Investigation, Resources, Writing – original draft, Vi- sualization, Supervision, Project administration, Funding acquisition. **Stephen C. Licht:** Conceptualization, Methodology, Software, Investi- gation, Data curation, Writing – review & editing, Supervision. **Roberto Belotti:** Software, Validation, Formal analysis, Investigation, Data cu- ration, Writing – review & editing, Visualization. **Helen C. Henninger:** Formal analysis, Investigation, Writing – review & editing.

Declaration of competing interest

The authors declare that they have no known competing finan- cial interests or personal relationships that could have appeared to influence the work reported in this paper.

Acknowledgment

The authors would like to thank the Federazione Sudtirolese All- evatori Razze Bovine for kindly allowing them access to its parking facility.

References

[1] Musić S, Hirche S. Control sharing in human-robot team interaction. Ann Rev Control 2017;44:342–54.

[2] Angerer M, Musić S, Hirche S. Port-Hamiltonian based control for human-robot team interaction. In: Robotics and automation (ICRA), 2017 IEEE international conference on. IEEE; 2017, p. 2292–9.

[3] Franchi A, Secchi C, Ryll M, Bulthoff HH, Giordano PR. Shared control : Balancing autonomy and human assistance with a group of quadrotor UAVs. IEEE Robot Autom Mag 2012;19(3):57–68. http://dx.doi.org/10.1109/MRA.2012.2205625.

[4] Han J, Park J, Kim T, Kim J. Precision navigation and mapping under bridges with an unmanned surface vehicle. Auton Robots 2015;38(4):349–62.

[5] von Ellenrieder KD. Development of a USV-based bridge inspection system. In: OCEANS'15 MTS/IEEE Washington. IEEE; 2015, p. 1–10.

[6] Ludvigsen M, Sørensen AJ. Towards integrated autonomous underwater operations for ocean mapping and monitoring. Ann Rev Control 2016;42:145–57.

[7] Bayat B, Crasta N, Crespi A, Pascoal AM, Ijspeert A. Environmental monitoring using autonomous vehicles: A survey of recent searching techniques. Curr Opin Biotechnol 2017;45:76–84.

[8] Ore J-P, Detweiler C. Sensing water properties at precise depths from the air. In: Field and service robotics. Springer; 2018, p. 205–20.

[9] Vidoni R, Bietresato M, Gasparetto A, Mazzetto F. Evaluation and stability comparison of different vehicle configurations for robotic agricultural operations on side-slopes. Biosyst Eng 2015;129:197–211.

[10] Bawden O, Kulk J, Russell R, McCool C, English A, Dayoub F, et al. Robot for weed species plant-specific management. J Field Robot 2017;34(6):1179–99.

[11] Geravand M, Werner C, Hauer K, Peer A. An integrated decision making approach for adaptive shared control of mobility assistance robots. Int J Soc Robot 2016;8(5):631–48.

[12] Gopinath D, Jain S, Argall BD. Human-in-the-loop optimization of shared autonomy in assistive robotics. IEEE Robot Automat Lett 2017;2(1):247–54.

[13] Profumo L, Pollini L, Abbink DA. Direct and indirect haptic aiding for curve negotiation. In: 2013 IEEE international conference on systems, man, and cybernetics. 2013, p. 1846–52. http://dx.doi.org/10.1109/SMC.2013.318.

[14] Nishimura R, Wada T, Sugiyama S. Haptic shared control in steering operation based on cooperative status between a driver and a driver assistance system. J Hum-Robot Interact 2015;4(3):19–37.

[15] Wada T, Sonoda K, Okasaka T, Saito T. Authority transfer method from automated to manual driving via haptic shared control. In: 2016 IEEE international conference on systems, man, and cybernetics. 2016, p. 002659–64. http://dx.doi.org/10.1109/SMC.2016.7844641.

[16] Ghasemi AH, Rastgoftar H. Adaptive haptic shared control framework using Markov decision processing. In: ASME 2018 dynamic systems and control conference. American Society of Mechanical Engineers; 2018, http://dx.doi.org/10.1115/DSCC2018-9009, V003T32A003.

[17] Flemisch FO, Adams CA, Conway SR, Goodrich KH, Palmer MT, Schutte PC. The H-Metaphor as a guideline for vehicle automation and interaction. Tech. rep. NASA/TM—2003-212672, NASA Langley Research Center, Hampton, Virginia; 2003.

[18] Flemisch F, Heesen M, Hesse T, Kelsch J, Schieben A, Beller J. Towards a dynamic balance between humans and automation: Authority, ability, responsibility and control in shared and cooperative control situations. Cogn, Technol Work 2012;14(1):3–18.

[19] Flemisch F, Canpolat Y, Altendorf E, Weßel G, Itoh M, Flemisch F, et al. Shared and cooperative control of ground and air vehicles: Introduction and general overview. In: 2017 IEEE international conference on systems, man, and cybernetics. 2017, p. 858–63. http://dx.doi.org/10.1109/SMC.2017.8122717.

[20] Jiang J, Astolfi A. Shared-control for fully actuated linear mechanical systems. In: 52nd IEEE conference on decision and control. 2013, p. 4699–704. http://dx.doi.org/10.1109/CDC.2013.6760625.

[21] Jiang J, Di Franco P, Astolfi A. Shared control for the kinematic and dynamic models of a mobile robot. IEEE Trans Control Syst Technol 2016;24(6):2112–24. http://dx.doi.org/10.1109/TCST.2016.2528890.

[22] Saeidi H, McLane F, Sadrfaidpour B, Sand E, Fu S, Rodriguez J, et al. Trust-based mixed-initiative teleoperation of mobile robots. In: 2016 American control conference. IEEE; 2016, p. 6177–82.

[23] Corredor J, Sofrony J, Peer A. Decision-making model for adaptive impedance control of teleoperation systems. IEEE Trans Haptics 2017;10(1):5–16.

[24] Hokayem PF, Spong MW. Bilateral teleoperation: An historical survey. Automatica 2006;42(12):2035–57.

[25] Mohammadi A, Marquez HJ, Tavakoli M. Nonlinear disturbance observers: Design and applications to Euler? Lagrange systems. IEEE Control Syst Mag 2017;37(4):50–72.

[26] von Ellenrieder KD, Henninger HC, Belotti R. Homogeneity for shared control in the presence of disturbances. IFAC-PapersOnLine 2019;52(15):235–40. http://dx.doi.org/10.1016/j.ifacol.2019.11.680, 8th IFAC Symposium on Mechatronic Systems MECHATRONICS 2019.

[27] Hindiyeh RY, Gerdes JC. Design of a dynamic surface controller for vehicle sideslip angle during autonomous drifting. IFAC Proc Vol 2010;43(7):560–5.

[28] Papoulias FA. Bifurcation analysis of line of sight vehicle guidance using sliding modes. Int J Bifur Chaos 1991;1(04):849–65.

[29] Borhaug E, Pavlov A, Pettersen KY. Cross-track formation control of underactuated surface vessels. In: Proceedings of the 45th IEEE conference on decision and control. IEEE; 2006, p. 5955–61.

[30] Breivik M, Fossen TI. Guidance laws for autonomous underwater vehicles. Underwater Veh 2009;4:51–76.

[31] Fossen TI. Handbook of marine craft hydrodynamics and motion control. John Wiley & Sons; 2011.

[32] Slotine J-JE, Li W, et al. Applied nonlinear control. prentice-Hall Englewood Cliffs, NJ; 1991.

[33] Shtessel Y, Edwards C, Fridman L, Levant A. Sliding mode control and observation. Springer; 2014.

[34] Levant A. Higher-order sliding modes, differentiation and output-feedback control. Int J Control 2003;76(9–10):924–41.

[35] Utkin VI, Poznyak AS. Adaptive sliding mode control with application to super-twist algorithm: Equivalent control method. Automatica 2013;49(1):39–47.

[36] Seeber R, Horn M. Guaranteeing disturbance rejection and control signal continuity for the saturated super-twisting algorithm. IEEE Control Syst Lett 2019;3(3):715–20.

[37] Seeber R, Horn M. Stability proof for a well-established super-twisting parameter setting. Automatica 2017;84:241–3.

[38] Oborne M. Ardupilot mission planner (v1.3.72). 2020, URL https://ardupilot.org/planner/. [Accessed 10 October].

[39] Meier L, Honegger D, Pollefeys M. PX4: A node-based multithreaded open source robotics framework for deeply embedded platforms. In: 2015 IEEE International conference on robotics and automation. IEEE; 2015, p. 6235–40.

[40] ArduPilot DevTeam. Ardupilot. 2020, URL http://www.ardupilot.org. [Accessed10 October].

